Letter

Light-hole gate-defined spin-orbit qubit

Patrick Del Vecchio and Oussama Moutanabbir [*]

Department of Engineering Physics, École Polytechnique de Montréal, C.P. 6079,
Succursale Centre-Ville, Montréal, Québec, Canada H3C 3A7

The selective confinement of light holes (LHs) is demonstrated by introducing a low-dimensional system consisting of a highly tensile-strained Ge quantum well enabling the design of an ultrafast gate-defined spin qubit under the electric dipole spin resonance. The qubit size-dependent *g* factor and dipole moment are mapped, and the parameters inducing their modulation are discussed. It is found that the LH qubit dipole moment is two to three orders of magnitude higher than that of the canonical heavy-hole qubit. This behavior originates from the significant spin splitting resulting from the combined action of large cubic and linear Rashba spin-orbit interactions that are peculiar to LHs. The qubit relaxation rate is also affected by the strong spin-orbit interaction and follows typically a B^7 behavior. The proposed all-group IV, direct band-gap LH qubit provides an effective platform for a scalable qubit-optical photon interface sought after for long-range entanglement distribution and quantum networks.

Gated quantum dots (QDs) exploiting the strong spin-orbit interaction (SOI) of holes and their quiet quantum environment provide practical building blocks for quantum processors [1–11]. However, due to the restricted choice of low-dimensional systems (e.g., Ge/SiGe), current hole spin qubits are based predominately on heavy-hole (HH) spins [12]. Notwithstanding this progress, the ability to utilize light-hole (LH) spins would enable additional degrees of freedom to engineer qubits with extended functionalities. Indeed, LHs allow simple schemes for a direct mapping of superposition from a flying qubit to a stationary spin qubit [13] as well as a better resilience against charge noise [14] and an enhanced proximity-induced superconductivity transfer [15]. Additionally, LHs are also known to have strong SOI yielding fast Rabi oscillations [14]. Nevertheless, the development of LH qubits has been hampered by the lack of proper material systems. Here, we address this limitation and introduce a low-dimensional system to control LH states.

The selective confinement of LHs in Ge quantum well (QW) requires sufficiently high tensile strain, which can be achieved using the emerging germanium-tin (Ge$_{1-x}$Sn$_x$) alloys [16]. Ge/Ge$_{1-x}$Sn$_x$ hole spin devices combine all advantages that are inherent to group IV semiconductors [17,18]. Besides the weaker hyperfine interaction with the surrounding nuclear spin bath resulting from the *p* symmetry of the hole wave function [19–21], the strong SOI in the valence band of Ge and Sn would enable all-electrical driving of the qubit without the need for an external rf transmission line and create rich spin-related phenomena unique to holes [22,23]. Moreover, the Ge$_{1-x}$Sn$_x$ alloy spans a wide range of lattice parameters [24–26], which is useful to control the hole spin properties through the epitaxial strain directly on silicon wafers [16,27,28].

Figure 1 illustrates the gate-defined LH QD. Note that the lattice mismatch between Ge and Ge$_{1-x}$Sn$_x$ induces a significant tensile strain in the Ge layer, which lifts the HH-LH degeneracy yielding a LH-like valence band edge [Fig. 1(b)]. The Ge$_{1-x}$Sn$_x$/Ge/Ge$_{1-x}$Sn$_x$ heterostructure confines LHs in the Ge layer for *x* typically higher than 0.11, while the HHs are pulled into the Ge$_{1-x}$Sn$_x$ barriers [16]. A set of electrostatic gates on top of the heterostructure helps confine the LH in the plane by applying a dc voltage. Note that Ge becomes a direct band-gap semiconductor at a tensile strain higher than 1.8%. The electric dipole spin resonance (EDSR) is performed by applying a microwave voltage. A feature that is sometimes neglected [29–31] but needs to be accounted for in this system is the spread of the LH wave function into the barriers. Because the HHs are located in the barriers, LH-HH mixing wave-function overlap only occurs outside the QW. Assuming a hard wall potential at the interface is therefore equivalent to neglecting entirely the LH-HH mixing. Moreover, the LH subband dispersion nonparabolicity must also be considered. The theoretical framework below for the in-plane motion of the LHs explicitly takes into account these peculiar features.

Eight-band $k \cdot p$ theory [33] is used for the derivation of an effective Hamiltonian for the two-dimensional (2D) LH gas incorporating the Bir-Pikus Hamiltonian and thus the effects of biaxial epitaxial strain [34]. [001]-oriented substrates are considered, with the growth direction parallel to the *z* axis. The operator ordering between material parameters and wave-vector components require special care to avoid spurious solutions and to properly include the effects of an external magnetic field [35,36]. An out-of-plane magnetic field $\mathbf{B} = B\mathbf{e}_z$ results in the following commutation relations for the mechanical wave-vector components: $[K_\alpha, K_\beta] = \epsilon_{\alpha\beta,z}/i\lambda^2$, where ϵ is the Levi-Civita tensor, $\lambda = \sqrt{\hbar/eB}$ is the magnetic length, and $\alpha, \beta = \{x, y, z\}$. The mechanical wave vector $\mathbf{K} = \mathbf{k} + e\mathbf{A}/\hbar$ is given in terms of the canonical wave vector $\mathbf{k} \rightarrow -i\nabla$. In the symmetric gauge, the vector potential $\mathbf{A} = B/2(-y\mathbf{e}_x + x\mathbf{e}_y)$.
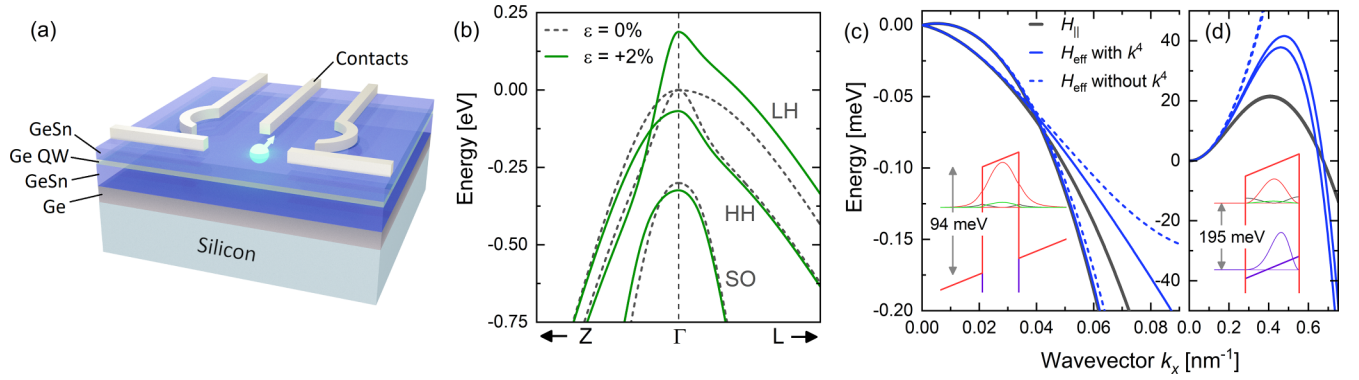
*oussama.moutanabbir@polymtl.ca

FIG. 1. (a) Schematic of a gate-defined Ge/Ge$_{1-x}$Sn$_x$ LH qubit. (b) Band structure of the valence band in bulk Ge without strain (dashed lines) and with 2% tensile strain (solid lines). $k \cdot p$ parameters taken from Ref. [32]. (c), (d) Ground LH subband dispersion from the numerical diagonalization of $H_\parallel$ (black solid lines) and from H_{eff} with (without) k^4 terms in solid (dashed) blue. (c) Ge/Ge$_{1-x}$Sn$_x$ LH QW with $E_z = 1$ MV/m. (d) Infinite Ge LH QW with $E_z = 5$ MV/m. Energy scale is in meV in both panels. Insets show the envelope probability density of the lowest subband [ground HH subband is also shown in (d)]. The larger component of the wave function is the LH part of the spinor (red). The smaller component with one lobe corresponds to the SO part (green) and the component with two small lobes at the Ge interfaces corresponds to the conduction band (CB) part (black). The tensile strain in Ge is 2.38% in both cases corresponding to $x = 0.15$.

The total Hamiltonian $H_\parallel$ for the in-plane motion of holes and electrons is written as a sum of different contributions [36], $H_\parallel = H_{k \cdot p}(\mathbf{K}_\parallel; k_z) + V(z)$, where $\mathbf{K}_\parallel = K_x \mathbf{e}_x + K_y \mathbf{e}_y$, $H_{k \cdot p}$ is the eight-band $k \cdot p$ matrix including strain and magnetic effects [33,36,37], and $V(z)$ is the band alignment. This last term also includes the effects of an out-of-plane electric field $\mathbf{E} = E_z \mathbf{e}_z$. The first step to find an effective LH Hamiltonian is to calculate the envelope functions and energies of $H_\parallel$ at $K_x = K_y = 0$ and $B = 0$. This provides an orthonormal basis (a set of subband edges) on which $H_\parallel$ is projected at finite $\mathbf{K}_\parallel$ and $B > 0$. This orthonormal basis contains two types of subbands. The first are pure HH subbands (H subbands) and the second are superpositions of LH, SO holes, and conduction band (CB) electrons (η subbands),

$$|H; l, \sigma\rangle = \left|\frac{3}{2}, \frac{3\sigma}{2}\right\rangle |l\rangle_h, \tag{1a}$$

$$|\eta; j, \sigma\rangle = \left|\frac{1}{2}, \frac{\sigma}{2}\right\rangle_c |j\rangle_c + \left|\frac{3}{2}, \frac{\sigma}{2}\right\rangle |j\rangle_\ell + \sigma \left|\frac{1}{2}, \frac{\sigma}{2}\right\rangle |j\rangle_s, \tag{1b}$$

where l and j are respectively the subband indices for H and η subbands and $\sigma = \pm 1$ is the pseudospin index. The first ket in each term represents bulk Bloch functions at the Γ point, while the second ket represents the envelope functions. The labels h, c, ℓ, s refer to the HH, CB, LH, and SO part of the spinor, respectively. Because subbands are either of type H or η, a "LH" subband is understood as an η subband such that $_\ell\langle j|j\rangle_\ell > _c\langle j|j\rangle_c$ and $_\ell\langle j|j\rangle_\ell > _s\langle j|j\rangle_s$. Following the projection of $H_\parallel$ upon the basis $\{|\eta\rangle, |H\rangle\}$, a fourth-order Schrieffer-Wolff transformation [38] is applied leading to an effective Hamiltonian for η subbands,

$$
\begin{aligned}
H_{eff} = {} & \alpha_0 \tilde{\gamma} K_\parallel^2 + \frac{\alpha_0}{\lambda^2} \frac{\tilde{g}}{2} \sigma_z + \alpha_0^2 \tilde{\gamma}' K_\parallel^4 + \frac{\alpha_0^2}{\lambda^4} \tilde{g}' + \frac{\alpha_0^2}{\lambda^2} \gamma_\lambda K_\parallel^2 \sigma_z \\
& + \alpha_0^2 [(\zeta K_-^4 + \text{H.c.})\sigma_+\sigma_- + (\zeta K_+^4 + \text{H.c.})\sigma_-\sigma_+] \\
& + i\beta_1 (K_-\sigma_+ - K_+\sigma_-) - i\beta_2 (K_+^3\sigma_+ - K_-^3\sigma_-) \\
& + i\beta_3 (K_-K_+K_-\sigma_+ - K_+K_-K_+\sigma_-), \tag{2}
\end{aligned}
$$

with $\alpha_0 = \hbar^2/(2m_0)$, m_0 the free-electron mass, $K_\pm = K_x \pm iK_y$, $\sigma_\pm = (\sigma_x \pm i\sigma_y)/2$, and $\sigma_{x,y,z}$ the Pauli matrices. The first term in (2) corresponds to the parabolic contribution in the dispersion relation, with $\tilde{\gamma}$ the effective mass parameter. The second term corresponds to the linear Zeeman splitting, with $\tilde{g}$ the effective g factor. The next three terms correspond to nonparabolicity ($\tilde{\gamma}'$), Zeeman splitting nonlinearity ($\tilde{g}'$), and a hybrid term proportional to $K_\parallel^2/\lambda^2$. The band-structure anisotropy is taken into account by the ζ parameter. Finally, the last three terms correspond to the linear Rashba splitting (β_1) and two kinds of cubic Rashba splitting (β_2 and β_3). The effective parameters in (2) in terms of the envelopes $|l\rangle_h$ and $|j\rangle_{c,\ell,s}$ are presented in the Supplemental Material (SM) [37]. This approach is similar to that employed by Refs. [29–31] for instance. However, here the spread of the wave function into the barriers and the effects of $\mathbf{E}$ are implicitly taken into account from the shape of the envelopes, and the effective parameters in (2) are calculated from a larger subband edge basis due to the large amount of HH levels in the barriers. Figure 1 shows the dispersion of the ground LH subband for two different QWs. Figure 1(c) displays the case of a 13-nm Ge QW with relaxed Ge$_{0.85}$Sn$_{0.15}$ barriers. Close to $k_\parallel = 0$, H_{eff} fits exactly $H_\parallel$ because the effective parameters in (2) are given exactly by fourth-order perturbation theory. H_{eff} diverges from $H_\parallel$ further away from $k_\parallel = 0$ because k^5 terms or higher become important. This behavior is exacerbated for a QW with infinite band offsets [Fig. 1(d)]. In both cases, H_{eff} diverges faster when k^4 terms are neglected.

The calculations also predict an effective mass for the ground LH subband of the opposite sign [clearly visible in Fig. 1(d)] for certain QW parameters. Such behavior was also observed for different material systems [39–41]. This effect becomes more prominent as the QW thickness decreases. The typical holelike dispersion is recovered above a critical thickness, corresponding to 11 nm for the Ge/GeSn QW system in Fig. 1(c). To simplify the LH qubit calculations, the thickness is fixed at 13 nm.

The QD Hamiltonian includes the isotropic and parabolic confinement from the top gates, $H_{QD} = H_{eff} + m^* \omega_0^2$

$(x^2 + y^2)/2$, where $m^* = m_0/\tilde{\gamma}$ is the in-plane effective mass. H_{QD} is diagonalized by first writing $H_{QD} = H_0 + H'$, where H_0 consists of the first two terms in (2) plus the parabolic confinement,

$$H_0 = \alpha_0 \tilde{\gamma} K_\parallel^2 + \frac{1}{2} m^* \omega_0^2 (x^2 + y^2) + \frac{\alpha_0}{\lambda^2} \frac{\tilde{g}}{2} \sigma_z \qquad (3)$$

$$= \hbar\omega_l (a_1^\dagger a_1 + a_2^\dagger a_2 + 1) + \frac{\hbar\omega_c}{2} (a_1^\dagger a_1 - a_2^\dagger a_2)$$

$$+ \frac{\alpha_0}{\lambda^2} \frac{\tilde{g}}{2} \sigma_z, \qquad (4)$$

where

$$a_1 = \frac{x - iy}{2r} + \frac{irk_-}{2}, \quad a_2 = \frac{x + iy}{2r} + \frac{irk_+}{2} \qquad (5)$$

are ladder operators, $k_\pm = k_x \pm ik_y$, $\omega_c = eB/m^*$, $\omega_l^2 = \omega_0^2 + \omega_c^2/4$, and $r = \sqrt{\hbar/(m^*\omega_l)}$ is the effective quantum dot radius [37]. The eigenstates of H_0, the so-called Fock-Darwin orbitals $|n_1, n_2, \sigma\rangle$ with $n_{1,2} = 0, 1, \dots$ and $\sigma = \pm 1$, provide an orthonormal basis on which H_{QD} is projected. The eigenvalues of the resulting matrix for H_{QD} in the Fock-Darwin basis are then solved numerically. The two lowest-energy orbitals $|\mathbb{0}\rangle$ and $|\mathbb{1}\rangle$ corresponding to energies $E_\mathbb{0}$ and $E_\mathbb{1}$ define the qubit. These are mostly composed of the Fock-Darwin orbitals $|0, 0, -\rangle$ and $|0, 0, +\rangle$ respectively, plus higher-energy orbitals,

$$|\mathbb{0}\rangle = |0, 0\rangle |-\rangle + \left(c_{0,1}^{(\mathbb{0})} |0, 1\rangle + c_{3,0}^{(\mathbb{0})} |3, 0\rangle + c_{1,2}^{(\mathbb{0})} |1, 2\rangle\right) |+\rangle, \qquad (6a)$$

$$|\mathbb{1}\rangle = |0, 0\rangle |+\rangle + \left(c_{1,0}^{(\mathbb{1})} |1, 0\rangle + c_{0,3}^{(\mathbb{1})} |0, 3\rangle + c_{2,1}^{(\mathbb{1})} |2, 1\rangle\right) |-\rangle. \qquad (6b)$$

The coefficients $c_{n_1,n_2}^{(\mathbb{0},\mathbb{1})}$ were extracted from the numerical diagonalization of H_{QD} to avoid artifacts near crossings between Fock-Darwin orbitals. They can be evaluated with perturbation theory away from these crossings [37]. For a driving field $\tilde{\mathbf{E}}(t) = \mathbf{e}_x E_{AC} \cos(\omega t)$, where $\hbar\omega = |E_\mathbb{0} - E_\mathbb{1}|$ is the qubit energy, the Rabi frequency Ω is given in terms of the qubit dipole moment $d = e\langle\mathbb{0}| x |\mathbb{1}\rangle$ by $\Omega = E_{AC}|d|/\hbar$.

Figure 2 shows the QD orbital energies as a function of the out-of-plane magnetic field for a QD radius $r_0 = \sqrt{\hbar/m^*\omega_0} = 25$ nm and the same QW parameters as in Fig. 1(a). The qubit undergoes a transition from a spin qubit to a charge qubit at the crossing between $|\mathbb{1}\rangle$ and the mostly $|0, 1, -\rangle$ orbital near $B = 0.275$ T. The two levels cross because $|0, 1, -\rangle$ is not present in the expansion of $|\mathbb{1}\rangle$.

The qubit dipole moment d and the qubit g factor $|g_{QD}|$ are plotted in Fig. 3 as a function of the QD radius r_0 and $B = 0.05$ T. The g factor has a strong dependence on r_0 for small radii, and approaches asymptotically the QW value $\tilde{g} = 8.69$ at large r_0. The large $\tilde{g}$ value originates from the first-order approximation $\tilde{g} \approx 2\kappa$ for a LH spin in a perpendicular magnetic field with $\kappa = 3.41$ in Ge. Deviations from 2κ come from the spread of the wave function and second-order corrections [37,42]. The dipole moment d takes very large values for two main reasons. First, the coefficient β_3 that contributes to EDSR by introducing a $|1, 0, -\rangle$ contribution into $|\mathbb{1}\rangle$ depends on the sum $(\gamma_2 + \gamma_3)$ for LHs [37] whereas for HHs it depends on the difference $(\gamma_2 - \gamma_3)$. In Ge, $\gamma_2 \approx \gamma_3$ [43] and therefore
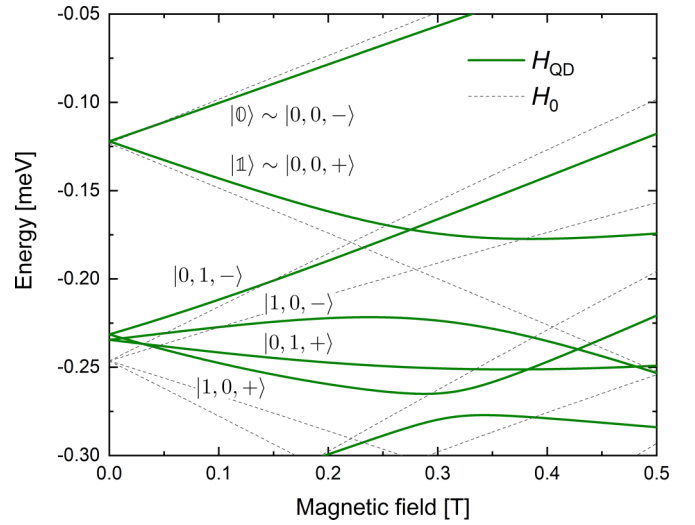

FIG. 2. LH QD orbital energies as a function of B. The QD radius r_0 at $B = 0$ is kept constant at 25 nm. Black dotted lines represent the eigenvalues of H_0, while the solid green lines are those of H_{QD}. The qubit levels $|\mathbb{0}\rangle$ and $|\mathbb{1}\rangle$ and excited orbitals are displayed with their main contributions from the eigenstates $|n_1, n_2, \sigma\rangle$ for $B = 0.1$ T. The QW parameters are the same as in Fig. 1(c).

β_3 is much larger for LHs. Second, LHs are subject to a linear Rashba spin splitting proportional to β_1, which is nonexistent for HHs. This additional term contributes to a large d similarly to β_3 by increasing the contribution of $|1, 0, -\rangle$ into $|\mathbb{1}\rangle$. At ≈ 27.5 nm, $|d|$ reaches a maximum as a result of the combined effects of β_1 and β_3, which gives a dipole moment that is two to three orders of magnitude larger than that of HHs in a compressively strained Ge [29,44]. For instance, an in-plane driving field as small as $E_{AC} = 1$ mV/μm gives a Rabi frequency $\Omega \approx 1.2$ GHz.

There is, however, a range of QD radii where the dipole moment is very small (Fig. 3). This happens because both β_1 and β_3 contribute to d. When B is small such that $|\mathbb{1}\rangle$ is far
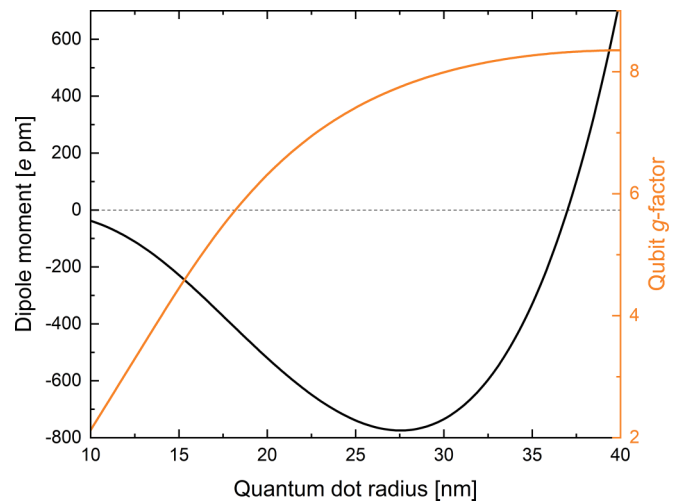

FIG. 3. LH qubit dipole moment (left) and absolute value of the g factor (right) as a function of the QD radius r_0. The magnetic field is fixed at 0.05 T. The QW parameters are the same as in Fig. 1(c).
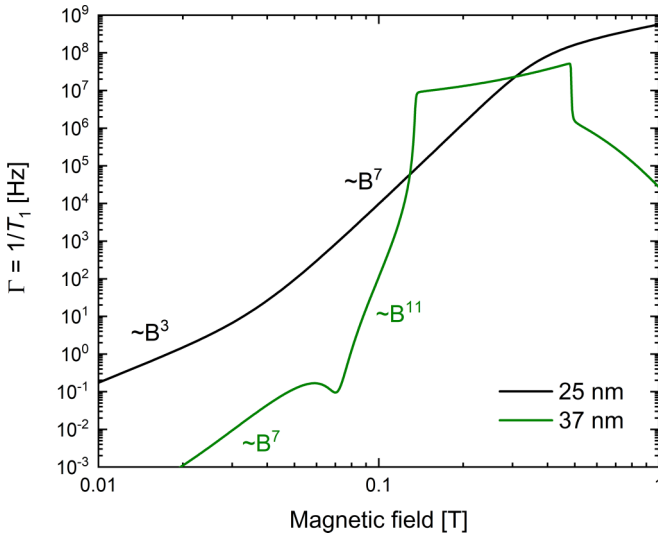
FIG. 4. Relaxation rate $\Gamma = 1/T_1$ as a function of the magnetic field. The QW parameters are the same as in Fig. 1(c).

from the excited orbitals, the dipole moment is given by

$$|d| \approx \frac{em^{*2}r^2|\tilde{g}|\mu_\mathrm{B}B}{\hbar^4}\left|r^2\beta_1 + 2\beta_3\right|. \qquad (7)$$

Therefore, when $\beta_1\beta_3 < 0$, d can vanish at specific values of r_0 and B. For the QW parameters in Fig. 1(a), $\beta_1 = 0.42$ meV nm and $\beta_3 = -290$ meV nm^3 which causes the dipole moment to vanish at $B = 0.05$ T and $r_0 \approx 37$ nm. For $r_0 > 37$ nm, d increases again, but at the cost of a smaller orbital energy spacing.

An important feature of LH qubits is that EDSR is driven by both η-H and η-η mixing. This is because there is an allowed first-order coupling between η subbands $\langle \eta; j, + | H_\parallel | \eta; j', - \rangle = R_{j,j'}K_-$ that is nonexistent for HHs [37]. The η-H mixing part contributes mainly to the β_3 parameter through a term proportional to $(\gamma_2 + \gamma_3)$, while η-η mixing contributes to both β_3 and β_1. Notably, these two types of mixing are of equal importance given that β_1 and β_3 can interfere to suppress the dipole moment [cf. (7)].

The relaxation time $T_1 = 1/\Gamma$ of the LH qubit was also evaluated for the system in Fig. 1(a). The coupling of the hole to acoustic phonons was considered. The total relaxation rate $\Gamma = \Gamma_\mathrm{em} + \Gamma_\mathrm{abs}$, where Γ_em (Γ_abs) is the rate associated with the emission (absorption) of one phonon. Each of these rates is calculated by Fermi's golden rule,

$$\Gamma_i = \frac{2\pi\mathcal{V}}{\hbar}\sum_\alpha\int\frac{d^3q}{8\pi^3}|\langle f | W_\alpha | i\rangle|^2\delta(\hbar\omega - \hbar\omega_{\alpha\mathbf{q}}), \qquad (8)$$

where $\mathcal{V}$ is the volume of the system and $\hbar\omega_{\alpha\mathbf{q}} = \hbar v_\alpha q$ is the phonon energy in branch $\alpha = \{\mathrm{LA,TA1,TA2}\}$ and with momentum $\mathbf{q} = q\hat{\mathbf{q}}$. $|i, f\rangle$ represent initial and final qubit levels

upon absorption or emission of a phonon. The operator W_α is derived from the hole-phonon Hamiltonian in a procedure similar to that in Refs. [31,45–47]. See SM [37] for details. Importantly, the matrix element $\langle f | W_\alpha | i\rangle$ takes into account the relaxation rate associated with all three spin-orbit parameters β_1, β_2, and β_3.

Figure 4 shows the computed Γ as a function of B for the Ge/GeSn QW system in Fig. 1(a) at $r_0 = 25$ nm. A relaxation time $T_1 = 100$ μs was extracted at $B = 0.1$ T. Moreover, Γ follows a B^7 behavior when $B \gg \sqrt{12}k_\mathrm{B}T/(g_\mathrm{QD}\mu_\mathrm{B})$ and a B^6 behavior when $B \ll \sqrt{12}k_\mathrm{B}T/(g_\mathrm{QD}\mu_\mathrm{B})$. This higher relaxation rate for LHs compared to HHs [12,31] is due to the larger spin-orbit coupling parameters $\beta_{1,2,3}$. The B^7 behavior at low temperature is associated to the spin-orbit term $|r^2\beta_1 + 2\beta_3|$ that was encountered in Eq. (7) and from the sum $c_{0,1}^{(0)} + c_{1,0}^{(1)} \sim B$.

Similar calculations were also performed at a QD radius $r_0 = 37.9$ nm for which the dipole moment vanishes at $B = 0.05$ T (Fig. 4). In this case, two different regimes were observed: For $B \ll 0.05$ T the relaxation rate exhibits a B^7 behavior, but at $B \gg 0.05$ T it evolves as $\sim B^{11}$. This is because the term associated with $|r^2\beta_1 + 2\beta_3|$ vanishes and the dominating terms in Γ are those associated with β_2, β_3 alone and the superposition coefficients $c_{n_1,n_2}^{(0,1)}$ with $n_1 + n_2 = 3$. At $B = 0.1$ T, $T_1 = 8$ ms, which is consistent with a much smaller dipole moment at this radius. The abrupt change in behavior around $B = 0.14$ T is due to a very small anticrossing between $|\mathbb{1}\rangle$ and the mostly $|1, 0, -\rangle$ orbital, while at $B = 0.5$ T it is caused by a small anticrossing between the mostly $|1, 0, -\rangle$ and the mostly $|0, 3, -\rangle$ orbital.

In conclusion, this Letter unravels the spin properties of a light-hole gated quantum dot in tensile strained Ge under EDSR. A detailed framework is described taking into account the spread of the envelopes in the barriers surrounding the quantum well and the effects of the dispersion nonparabolicity. It was found that light holes have a dipole moment d significantly larger than that of the heavy holes due to a larger cubic Rashba parameter (β_3) and the existence of a nonzero linear Rashba parameter (β_1). Interestingly, β_1 and β_3 can interfere destructively and cause the dipole moment to vanish at a specific quantum dot size. The relaxation rate Γ of a light-hole qubit follows a B^7 behavior, except when $d \approx 0$ where Γ follows a B^{11} behavior. This direct band-gap Ge/GeSn device structure provides additional degrees of freedom to implement silicon-compatible and scalable quantum processors leveraging the advantages of light-hole spin properties in addition to their efficient coupling with optical photons and their ability to transfer superconductivity.

[1] N. W. Hendrickx, W. I. L. Lawrie, L. Petit, A. Sammak, G. Scappucci, and M. Veldhorst, A single-hole spin qubit, Nat. Commun. **11**, 3478 (2020).

[2] N. W. Hendrickx, D. P. Franke, A. Sammak, G. Scappucci, and M. Veldhorst, Fast two-qubit logic with holes in germanium, Nature (London) **577**, 487 (2020).

[3] N. W. Hendrickx, W. I. L. Lawrie, M. Russ, F. van Riggelen, S. L. de Snoo, R. N. Schouten, A. Sammak, G. Scappucci, and M. Veldhorst, A four-qubit germanium quantum processor, Nature (London) **591**, 580 (2021).

[4] W. I. L. Lawrie, N. W. Hendrickx, F. van Riggelen, M. Russ, L. Petit, A. Sammak, G. Scappucci, and M. Veldhorst, Spin relaxation benchmarks and individual qubit addressability for holes in quantum dots, Nano Lett. **20**, 7237 (2020).

[5] A. Bogan, S. Studenikin, M. Korkusinski, L. Gaudreau, P. Zawadzki, A. Sachrajda, L. Tracy, J. Reno, and T. Hargett, Single hole spin relaxation probed by fast single-shot latched charge sensing, Commun. Phys. **2**, 17 (2019).

[6] D. Q. Wang, O. Klochan, J.-T. Hung, D. Culcer, I. Farrer, D. A. Ritchie, and A. R. Hamilton, Anisotropic Pauli spin blockade of holes in a GaAs double quantum dot, Nano Lett. **16**, 7685 (2016).

[7] H. Watzinger, J. Kukučka, L. Vukušić, F. Gao, T. Wang, F. Schäffler, J.-J. Zhang, and G. Katsaros, A germanium hole spin qubit, Nat. Commun. **9**, 3902 (2018).

[8] L. Vukušić, J. Kukučka, H. Watzinger, J. M. Milem, F. Schäffler, and G. Katsaros, Single-shot readout of hole spins in Ge, Nano Lett. **18**, 7141 (2018).

[9] D. Jirovec, P. M. Mutter, A. Hofmann, A. Crippa, M. Rychetsky, D. L. Craig, J. Kukucka, F. Martins, A. Ballabio, N. Ares, D. Chrastina, G. Isella, G. Burkard, and G. Katsaros, Dynamics of Hole Singlet-Triplet Qubits with Large g-Factor Differences, Phys. Rev. Lett. **128**, 126803 (2022).

[10] K. Wang, G. Xu, F. Gao, H. Liu, R.-L. Ma, X. Zhang, Z. Wang, G. Cao, T. Wang, J.-J. Zhang, D. Culcer, X. Hu, H.-W. Jiang, H.-O. Li, G.-C. Guo, and G.-P. Guo, Ultrafast coherent control of a hole spin qubit in a germanium quantum dot, Nat. Commun. **13**, 206 (2022).

[11] S. Bosco and D. Loss, Fully Tunable Hyperfine Interactions of Hole Spin Qubits in Si and Ge Quantum Dots, Phys. Rev. Lett. **127**, 190501 (2021).

[12] G. Scappucci, C. Kloeffel, F. A. Zwanenburg, D. Loss, M. Myronov, J.-J. Zhang, S. De Franceschi, G. Katsaros, and M. Veldhorst, The germanium quantum information route, Nat. Rev. Mater. **6**, 926 (2021).

[13] R. Vrijen and E. Yablonovitch, A spin-coherent semiconductor photo-detector for quantum communication, Physica E **10**, 569 (2001).

[14] J. C. Abadillo-Uriel and M. J. Calderón, Spin qubit manipulation of acceptor bound states in group IV quantum wells, New J. Phys. **19**, 043027 (2017).

[15] A. G. Moghaddam, T. Kernreiter, M. Governale, and U. Zülicke, Exporting superconductivity across the gap: Proximity effect for semiconductor valence-band states due to contact with a simple-metal superconductor, Phys. Rev. B **89**, 184507 (2014).

[16] S. Assali, A. Attiaoui, P. Del Vecchio, S. Mukherjee, J. Nicolas, and O. Moutanabbir, A light-hole germanium quantum well on silicon, Adv. Mater. **34**, 2201192 (2022).

[17] A. Hollmann, T. Struck, V. Langrock, A. Schmidbauer, F. Schauer, T. Leonhardt, K. Sawano, H. Riemann, N. V. Abrosimov, D. Bougeard, and L. R. Schreiber, Large, Tunable Valley Splitting and Single-Spin Relaxation Mechanisms in a Si/Si$_x$Ge$_{1-x}$ Quantum Dot, Phys. Rev. Appl. **13**, 034068 (2020).

[18] A. M. J. Zwerver, T. Krähenmann, T. F. Watson, L. Lampert, H. C. George, R. Pillarisetty, S. A. Bojarski, P. Amin, S. V. Amitonov, J. M. Boter, R. Caudillo, D. Correas-Serrano, J. P. Dehollain, G. Droulers, E. M. Henry, R. Kotlyar, M. Lodari, F. Lüthi, D. J. Michalak, B. K. Mueller *et al.*, Qubits made by advanced semiconductor manufacturing, Nat. Electron. **5**, 184 (2022).

[19] C. Testelin, F. Bernardot, B. Eble, and M. Chamarro, Hole–spin dephasing time associated with hyperfine interaction in quantum dots, Phys. Rev. B **79**, 195440 (2009).

[20] P. Machnikowski, K. Gawarecki, and L. Cywiński, Hyperfine interaction for holes in quantum dots: $k \cdot p$ model, Phys. Rev. B **100**, 085305 (2019).

[21] P. Philippopoulos, S. Chesi, and W. A. Coish, First-principles hyperfine tensors for electrons and holes in gaas and silicon, Phys. Rev. B **101**, 115302 (2020).

[22] R. Moriya, K. Sawano, Y. Hoshi, S. Masubuchi, Y. Shiraki, A. Wild, C. Neumann, G. Abstreiter, D. Bougeard, T. Koga, and T. Machida, Cubic Rashba Spin-Orbit Interaction of a Two-Dimensional Hole Gas in a Strained-Ge/SiGe Quantum Well, Phys. Rev. Lett. **113**, 086601 (2014).

[23] P. Del Vecchio, M. Lodari, A. Sammak, G. Scappucci, and O. Moutanabbir, Vanishing Zeeman energy in a two-dimensional hole gas, Phys. Rev. B **102**, 115304 (2020).

[24] O. Moutanabbir, S. Assali, X. Gong, E. O'Reilly, C. A. Broderick, B. Marzban, J. Witzens, W. Du, S.-Q. Yu, A. Chelnokov, D. Buca, and D. Nam, Monolithic infrared silicon photonics: The rise of (Si)GeSn semiconductors, Appl. Phys. Lett. **118**, 110502 (2021).

[25] M. P. Polak, P. Scharoch, and R. Kudrawiec, The electronic band structure of Ge$_{1-x}$Sn$_x$In the full composition range: indirect, direct, and inverted gaps regimes, band offsets, and the Burstein–Moss effect, J. Phys. D **50**, 195103 (2017).

[26] *Semiconductors, Group IV Elements and III-V Compounds*, edited by O. Madelung (Springer, Berlin, 1991).

[27] D. Stange, N. von den Driesch, D. Rainko, C. Schulte-Braucks, S. Wirths, G. Mussler, A. T. Tiedemann, T. Stoica, J. M. Hartmann, Z. Ikonic, S. Mantl, D. Grützmacher, and D. Buca, Study of GeSn based heterostructures: towards optimized group IV MQW LEDs, Opt. Express **24**, 1358 (2016).

[28] M. R. M. Atalla, S. Assali, S. Koelling, A. Attiaoui, and O. Moutanabbir, High-bandwidth extended-SWIR GeSn photodetectors on silicon achieving ultrafast broadband spectroscopic response, ACS Photonics **9**, 1425 (2022).

[29] L. A. Terrazos, E. Marcellina, Z. Wang, S. N. Coppersmith, M. Friesen, A. R. Hamilton, X. Hu, B. Koiller, A. L. Saraiva, D. Culcer, and R. B. Capaz, Theory of hole-spin qubits in strained germanium quantum dots, Phys. Rev. B **103**, 125201 (2021).

[30] D. V. Bulaev and D. Loss, Electric Dipole Spin Resonance for Heavy Holes in Quantum Dots, Phys. Rev. Lett. **98**, 097202 (2007).

[31] Z. Wang, E. Marcellina, A. R. Hamilton, J. H. Cullen, S. Rogge, J. Salfi, and D. Culcer, Optimal operation points for ultrafast, highly coherent Ge hole spin-orbit qubits, npj Quantum Inf. **7**, 54 (2021).

[32] D. Rideau, M. Feraille, L. Ciampolini, M. Minondo, C. Tavernier, H. Jaouen, and A. Ghetti, Strained Si, Ge, and Si$_{1-x}$Ge$_x$ alloys modeled with a first-principles-optimized full-zone $k \cdot p$ method, Phys. Rev. B **74**, 195208 (2006).

[33] E. O. Kane, Band structure of indium antimonide, J. Phys. Chem. Solids **1**, 249 (1957).

[34] G. Bir and G. Pikus, *Symmetry and Strain-Induced Effects in Semiconductors* (Wiley, New York, 1974).

[35] B. A. Foreman, Elimination of spurious solutions from eight-band $\mathbf{k} \cdot \mathbf{p}$ theory, Phys. Rev. B **56**, R12748 (1997).

[36] T. Eißfeller, Theory of the electronic structure of quantum dots in external fields, Ph.D. thesis, Technische Universitaet Muenchen, 2012.

[37] See Supplemental Material at http://link.aps.org/supplemental/10.1103/PhysRevB.107.L161406 for details on the $k \cdot p$ Hamiltonian, the subband edge basis, the subband parameters in the LH effective Hamiltonian, the solution of the QD Hamiltonian, the LH qubit relaxation rate, and the GeSn alloy material parametrization, which includes Refs. [48–54].

[38] R. Winkler, *Spin-Orbit Coupling Effects in Two-Dimensional Electron and Hole Systems*, Springer Tracts in Modern Physics (Springer, Berlin, 2003).

[39] D. Ahn and C. Shun-Lien, Optical gain in a strained-layer quantum-well laser, IEEE J. Quantum Electron. **24**, 2400 (1988).

[40] G. D. Sanders and Y.-C. Chang, Theory of photoabsorption in modulation-doped semiconductor quantum wells, Phys. Rev. B **35**, 1300 (1987).

[41] R. K. Hayden, D. K. Maude, L. Eaves, E. C. Valadares, M. Henini, F. W. Sheard, O. H. Hughes, J. C. Portal, and L. Cury, Probing the Hole Dispersion Curves of a Quantum Well Using Resonant Magnetotunneling Spectroscopy, Phys. Rev. Lett. **66**, 1749 (1991).

[42] Y. B. Lyanda-Geller, Spin-related phenomena in spin 3/2 charge carrier holes systems, Solid State Commun. **352**, 114815 (2022).

[43] D. J. Paul, 8-band $\mathbf{k} \cdot \mathbf{p}$ modelling of mid-infrared intersubband absorption in Ge quantum wells, J. Appl. Phys. **120**, 043103 (2016).

[44] B. Venitucci and Y.-M. Niquet, Simple model for electrical hole spin manipulation in semiconductor quantum dots: Impact of dot material and orientation, Phys. Rev. B **99**, 115317 (2019).

[45] J. Li, B. Venitucci, and Y.-M. Niquet, Hole-phonon interactions in quantum dots: Effects of phonon confinement and encapsulation materials on spin-orbit qubits, Phys. Rev. B **102**, 075415 (2020).

[46] D. V. Bulaev and D. Loss, Spin relaxation and anticrossing in quantum dots: Rashba versus Dresselhaus spin-orbit coupling, Phys. Rev. B **71**, 205324 (2005).

[47] L. M. Woods, T. L. Reinecke, and R. Kotlyar, Hole spin relaxation in quantum dots, Phys. Rev. B **69**, 125330 (2004).

[48] C. G. Van de Walle, Band lineups and deformation potentials in the model-solid theory, Phys. Rev. B **39**, 1871 (1989).

[49] D. V. Bulaev and D. Loss, Spin Relaxation and Decoherence of Holes in Quantum Dots, Phys. Rev. Lett. **95**, 076805 (2005).

[50] R. R. Reeber and K. Wang, Thermal expansion and lattice parameters of group IV semiconductors, Mater. Chem. Phys. **46**, 259 (1996).

[51] M. Bertrand, Q.-M. Thai, J. Chrétien, N. Pauc, J. Aubin, L. Milord, A. Gassenq, J.-M. Hartmann, A. Chelnokov, V. Calvo, and V. Reboud, Experimental calibration of Sn-related varshni parameters for high Sn content GeSn layers, Ann. Phys. **531**, 1800396 (2019).

[52] P. Lawaetz, Valence-band parameters in cubic semiconductors, Phys. Rev. B **4**, 3460 (1971).

[53] G. Chang, S. Chang, and S. L. Chuang, Strain-balanced Ge_zSn_{1-z}–$Si_xGe_ySn_{1-x-y}$ multiple-quantum-well lasers, IEEE J. Quantum Electron. **46**, 1813 (2010).

[54] K. Lu Low, Y. Yang, G. Han, W. Fan, and Y.-C. Yeo, Electronic band structure and effective mass parameters of $Ge_{1-x}Sn_x$ alloys, J. Appl. Phys. **112**, 103715 (2012).